Gastight Rotating Cylinder Electrode: Towards Decoupling Mass Transport and Intrinsic Kinetics in Electrocatalysis

Joonbaek Jang,[a] Martina Rüscher,[a] Maximilian Winzely,[a] and Carlos G. Morales-Guio[a,*]

[a] Department of Chemical and Biomolecular Engineering, University of California, Los Angeles, CA 90095, United States

Corresponding author: Morales-Guio, Carlos G. (moralesguio@ucla.edu)

Abstract

Decoupling and understanding the various mass, charge and heat transport phenomena involved in the electrocatalytic transformation of small molecules (i.e. CO_2, CO, H_2, N_2, NH_3, O_2, CH_4) is challenging but it can be readily achieved using dimensionless quantities (i.e. Reynolds, Sherwood, Schmidt, Damköhler, Nusselt, Prandtl, and Peclet Numbers) to simplify the characterization of systems with multiple interacting physical phenomena. Herein we report the development of a gastight rotating cylinder electrode cell with well-defined mass transport characteristics that can be applied to experimentally decouple mass transfer effects from intrinsic kinetics in electrocatalytic systems. The gastight rotating cylinder electrode cell enables the dimensionless analysis of electrocatalytic systems and should enable the rigorous research and development of electrocatalytic technologies.

Keywords:

Electrocatalysis, Reactor Design, Reaction Kinetics

1 INTRODUCTION

The development of devices for the electrochemical activation and transformation of small molecules such as CO_2, CO, N_2, CH_4 and H_2O into fuels, chemicals and fertilizers at global scales is a promising approach to the utilization of increasingly ubiquitous renewable electricity and the reduction of carbon emissions associated with the chemical process industries.[1-3] The electrification of chemical production systems and the realization of technologies capable of operating at global scales will depend not only on the demonstration of active and selective electrocatalysts in the laboratory, but also on the understanding of the mass, heat and charge transfer phenomena involved so that these systems can be one day scaled-up and commercialized. In studying the kinetics of small molecule activation on the surface of an electrode, it is essential to evaluate the relative contributions of mass transfer and true surface reactions. Such a distinction has been fundamental to the development and industrialization of thermo-catalytic processes and the theory of heterogeneous catalysis in general. In electrocatalysis, particularly for transformations that involve gas phase reactants, the distinction between intrinsic kinetics and mass transport limited kinetics has not been achieved due to the low solubility of gases in the electrolyte, competing homogeneous reactions involving these substrates and the lack of electrochemical cells with well-defined transport characteristics. Together, these factors have limited our understanding of the role of mass transport in electrocatalysis and hindered the advancement of the field.[4]

In order to gain insights into fundamental electrocatalytic reaction kinetics and to create a basis for the rational design of electrochemical reactors, we have developed a

gastight rotating cylinder electrode (RCE) cell that allows the detection and quantification of gas and liquid products generated on rotating cylinder electrodes under the conditions of well-defined hydrodynamics (Figure 1). The cylinder electrode area in the RCE gastight cell is 15 times larger than those common to rotating disk (RDE) electrodes (disk areas are typically around 0.2 cm^2) and because of its geometry, the RCE does not suffer from surface blockage from bubbles evolved in the process which has been a limiting factor for RDE systems.[5] The large geometric area to electrolyte volume in the gas-tight RCE cell results in detection limits for liquid products in the order of few μM in hour-long experiments and the on-line detection of gas products in the order of 1 ppm which are equivalent to partial current densities of less than 10 $\mu A\ cm^{-2}$. The gastight rotating cylinder electrode system presented here offers access to the rigorous study of electrode kinetics even at low current densities in low roughness, idealized electrodes. In this first description of the gastight rotating cylinder electrode

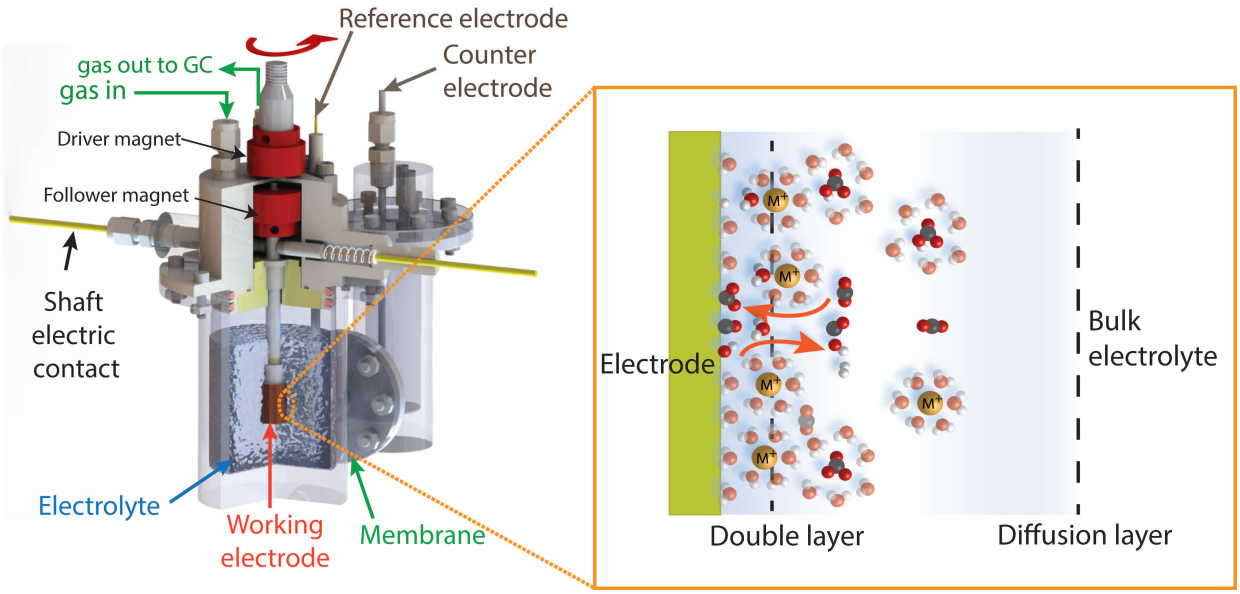

Figure 1. Schematic of the gas-tight rotating cylinder electrode cell prototype.

cell construction, we report on the quantification of products generated during various electrocatalytic transformations of an industrial interest such as the electrochemical hydrogen evolution, nitrite reduction to ammonia, and the carbon dioxide reduction to fuels and chemicals. In this work, we also demonstrate the combination of dimensionless analysis along with experiments under well-defined condition of mass transport to show that the reduction of CO_2 to C_1 and C_{2+} alcohols and hydrocarbons on polycrystalline copper electrodes is a first-order reaction process on the local concentration of CO, the main reaction intermediate. We show that the residence time of CO near the surface of the electrode is controlled by mass transport and that changing the residence time of CO is sufficient to change product selectivity without changing the electrode intrinsic kinetics.

2 ELECTROCHEMICAL CELL DESIGN

2.1 Prototype Cell Design

The first prototype of the gas-tight rotating cylinder electrode cell (Figure 1) is based on the design introduced by Jung *et al.*[6] where a follower magnet inside the cell traces, via magnetic coupling, a driver magnet outside the cell. The driver magnet is mounted on the shaft of a modulated speed rotator (MSR, Pine Research Instrumentation) with a range of rotation speeds that extends over 3000 rpm. The magnets (Magnetic Technologies, LTD.) are disc-shaped, and each consists of six alternating poles that allow the transmission of torque from the driver magnet to the follower magnet through air and the cap of the cell. The distance between the driver magnet and the top of the cap (air gap) is maintained close enough during operations to minimize lagging of the follower magnet. In order to determine the accuracy on the control of rotation speeds in

the gas-tight cell, the rotation speeds for both the driver and the follower magnets were measured using a tachometer (Pine Research Instrumentation) while varying the rotation speed from the modulated speed rotator (MSR). The rotation speeds of both magnets are the same for a broad range of rotation speeds (Figure 2). This indicates that the magnetic coupling is strong enough to transfer torque from the driver magnet to the follower magnet, and the rotation speed of the rotating electrode inside the gas-tight cell can be readily controlled from the MSR controller outside the cell.

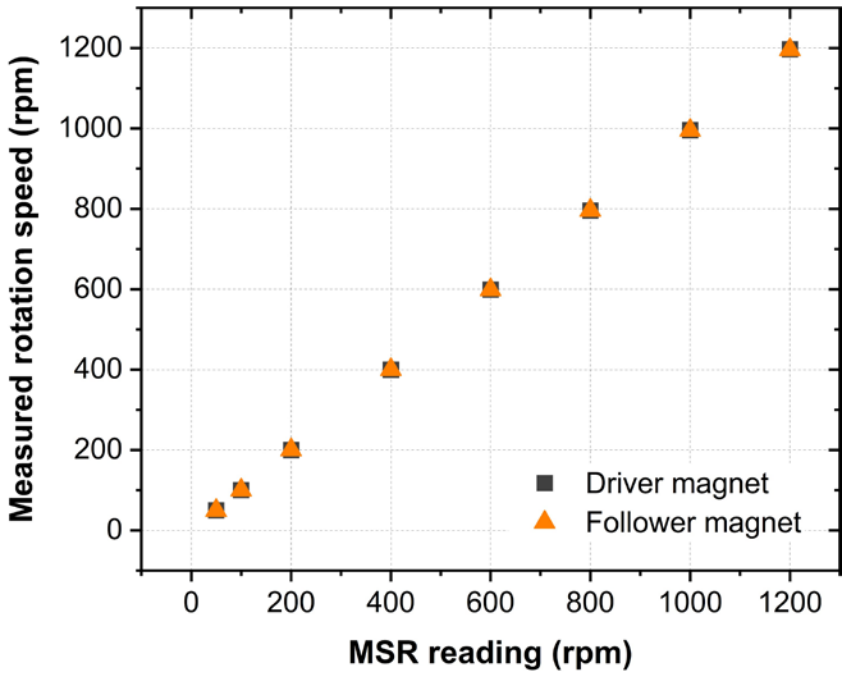

Figure 2. Rotation speeds of the driver (black square) and the follower magnet (orange triangle) measured using a tachometer while varying rotation speed from the modulated speed rotator (MSR).

The follower magnet is secured to a stainless-steel shaft tip (Pine Research Instrumentation) where the working electrode is mounted. This assembly rotates together while aligned centered through a sleeve bearing in the cell's cap. The cell cap contains the electrical connections and is designed to reduce the headspace above the electrolyte in the working electrode compartment. Reducing the headspace volume is

critical to shorten the time for produced gases to equilibrate within the working electrode compartment before injection into the gas chromatograph (GC) for their on-line detection and quantification.

The cap for the working electrode compartment has three threaded ports to accommodate leak-free gas fittings (Swagelok). One of these ports is used to bring in the gas feed into the cell and bubble it directly into the electrolyte. A second port serves as the gas outlet which transfers gas in the headspace out to the GC. The last threaded port on the top is an auxiliary port which can be used to introduce a second gas feed, measure the electrolyte temperature, or collect liquid aliquots during electrolysis. The cell's cap also holds a port for the reference electrode. Two threaded ports on the side of the cap allow the docking of custom-made cylinder blocks where commercially available spring-loaded silver-carbon brushes (Pine Research Instrumentation) can be positioned to make electric contact to the shaft. The brush contacts provide a stable electrical connection under rotation, while the other end of the spring is connected to the working electrode lead of the potentiostat through a stainless-steel rod. The prototype cell has an H-shape (Figure 1) where the working and counter electrode are separated by an ion conductive membrane. The cap for the counter electrode compartment only has three threaded ports from the top: one for the counter electrode, and the other two for the inlet and the outlet of gas. As in the original design by Jung *et al.*,[6] two O-rings between each compartment and its cap, and one O-ring between the working and the counter compartments are primarily responsible for ensuring a hermetic seal of the entire cell.

2.2 Second-Generation Gastight RCE Cell Design

While using the first prototype of the gas-tight rotating electrode cell, we sought for ways to improve the cell design. The main challenge encountered during the operation of the prototype version of the cell is the limitation in the current that can be achieved using the potentiostat due to a high overall cell resistance. A small cross section area of the membrane that separates the working and the counter electrodes limits the area available for ion transport between the electrodes and causes a large potential drop. This makes it difficult to explore high overpotential regimes especially when using lower concentration of the supporting electrolyte when the ionic conductivity is low.

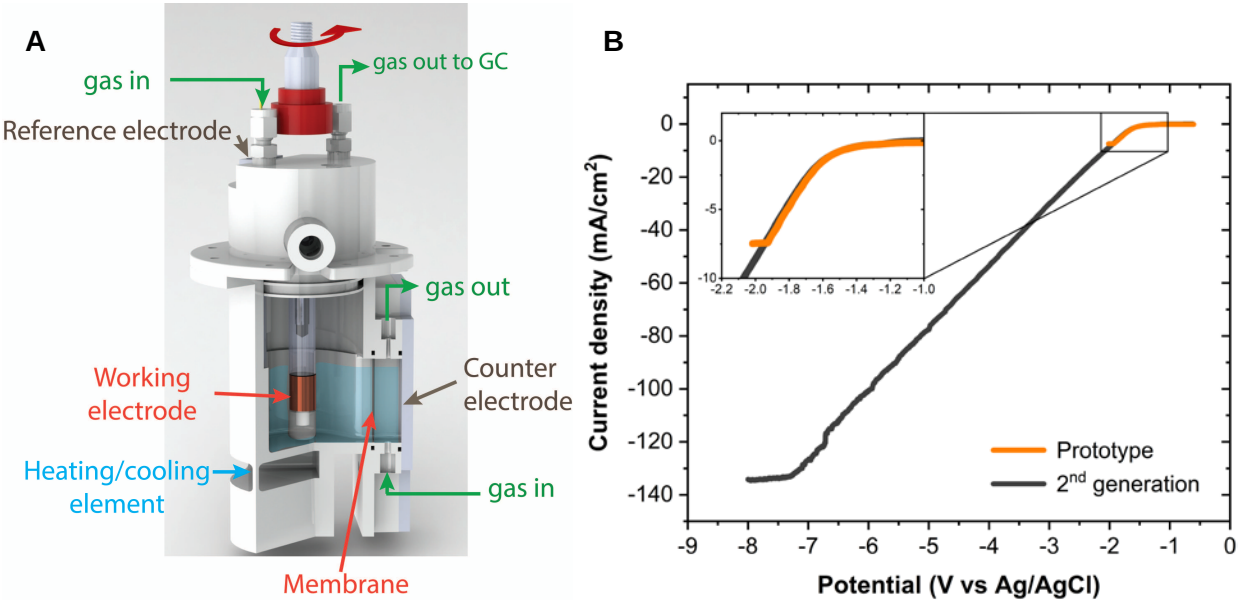

Figure 3. Second-generation gas-tight rotating cylinder electrode (RCE) cell design**. A)** Schematics of the 2nd generation cell with the modification to a compression-type counter electrode compartment and the addition of heating/cooling element. **B)** Current potential curve comparison for a 0.1M $KHCO_2$ solution in the prototype and 2nd generation RCE cell. Applied potential is not compensated for solution resistance. The maximum current is limited by the ion transport resistance between the working and counter electrode.

In the second-generation of the gas-tight rotating electrode cell, we have removed the channel that separated the two cell compartments and instead have attached the counter electrode as an auxiliary piece to the main body of the rotating cylinder through a compression design (Figure 3A). This compression type connection to the counter electrode side of the compartment resembles the design first introduced by Kuhl *et al.* for electrochemical CO_2 reduction,[1] which is now commonly used in fundamental electrocatalysis studies. In this modified counter electrode compartment, gas is bubbled from the bottom of the compartment and exits through the top of the middle plate, while the membrane and the counter electrode foil are compressed against the O-rings in between the working electrode compartment and the middle plate, and the middle plate to the end plate, respectively. Hex screws that go through the entire lower compartments and nuts are used to compress and hermetically seal the cell.

By removing the channel in the first prototype cell, we were able to shorten the distance between the working and the counter electrode while fully utilizing the wider cross-sectional area of the ion conductive membrane. The modified cell design was effective in reducing the overall cell resistance from the working electrode to the counter electrode, and as a result, the current density limit increased by around 18-fold, from 7.5 mA/cm^2 to 135 mA/cm^2 during electrolysis using a weakly buffered electrolyte solution (0.1 M potassium bicarbonate) commonly used in CO_2 electrocatalysis (Figure 3B). Another improvement that was made in this second-generation rotating electrode cell is the addition of a pocket beneath the electrolyte chamber on the working electrode side that can accommodate a cooling/heating element. This allows the control of the cell temperature to study the effect of temperature in the relative contributions on the

apparent reaction rate from the adsorption and desorption of reaction species, intrinsic reaction kinetics, and the mass and charge transfer properties. The cooling block with a heat-exchange area of 16 cm^2 was positioned 3.8 mm below the bottom of the RCE chamber on the working electrode side, and a bath circulator was used to circulate a 50/50 w/w ethylene glycol and water mixture in and out of the heating/cooling element. With this setup, it is possible to lower and equilibrate the electrolyte temperature inside the working electrode compartment down to 5 ^oC.

2.3 Solution Resistance Characterization

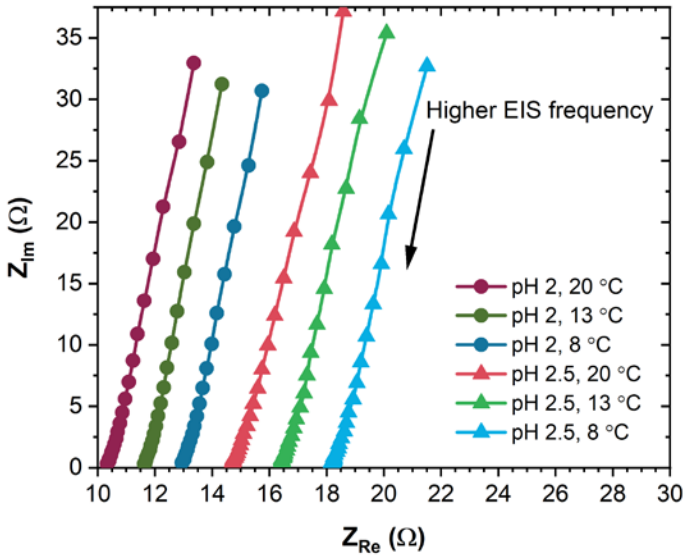

Figure 4. Impedance response as function of pH and temperature.

The potential drop between the potential applied to the surface of the electrode and the reference electrode will be a function of the solution conductivity. The conductivity of the solution is a function of the temperature, the ion concentration and the nature of the ion. The impedance response of two 0.05M $KClO_4$ solutions at different temperatures and pH, adjusted with the addition of $HClO_4$, is shown in Figure 4. The transference number of protons in the pH 2.0 and pH 2.5 electrolytes are t_{H^+}=0.31 and t_{H^+}=0.13, respectively

indicating that charge is predominantly carried in the bulk of the electrolyte by the K^+ and ClO_4^- ions. The difference in proton concentration is still enough to result in a higher solution resistance for the less acidic electrolyte. In addition, the solution resistance increases as the temperature of the cell decreases. The solution resistance measured at the high frequency end of the electrochemical impedance spectroscopy (EIS) spectrum is proportional to the distance between the reference and working electrode and inversely proportional to the active area of the electrode and the electrolyte conductivity. While all the physical dimensions of the working and reference electrode are kept constant, the change in temperature affects the ion diffusivity and thus affect conductivity between the working and reference electrode. It can be expected that temperature will also have a large effect on ion transport through the membranes used to separate the two cell compartments with higher cell temperatures likely contributing to the reduction of the cell potential to drive the same current density.[7]

3. RESULTS AND DISCUSSION

3.1 Mass Transport Characterization

The hydrodynamic conditions generated by the rotating cylinder electrode immersed in the electrolyte are quite turbulent even at low rotation rates. At very low rotation rates, the flow conditions near the surface of the electrode are laminar and quickly transitions to a turbulent flow as the rotation rate increases. The transition from laminar to turbulent flow for rotating cylinder electrodes is characterized using the Reynolds number that quantifies the ratio between inertial forces and viscous forces in the solution. For our rotating cylinder with outer diameter d_{cyl}= 1.2 cm, the Reynolds number is:

$$Re_{RCE} = U_{cyl} d_{cyl} \frac{\rho}{\mu} \quad (1)$$

where ρ is the solution density, and μ is the solution viscosity. The peripheral velocity of the rotating cylinder U_{cyl} is proportional to the rotation speed and the diameter and is given by Equation 2:

$$U_{cyl} = \omega \frac{d_{cyl}}{2} = \frac{\pi d_{cyl} f}{60} \quad (2)$$

where the rate can either be expressed as a function of the angular rotation rate, ω in rad/s, or the frequency f in revolutions per minute (rpm).

In this work, we have used the electrochemical reduction of ferricyanide (Equation 3), protons (Equation 4) and nitrite (Equation 5) to characterize the mass transfer properties of the cell.[8] See Supporting Information for experimental details on the preparation of electrolytes and the pre-treatment of electrodes.

$$[Fe(CN)_6]^{3-} + e^- \rightleftharpoons [Fe(CN)_6]^{4-} \quad (3)$$

$$2H^+ + 2e^- \rightleftharpoons \mathrm{H_2} \quad (4)$$

$$NO_2^- + 5\mathrm{H_2O} + 6e^- \rightleftharpoons \mathrm{NH_3} + 7OH^- \quad (5)$$

The reduction of ferricyanide, nitrite and protons are facile reactions resulting in the observed partial current to be solely limited by mass transfer at high overpotentials. The measured diffusion-limited current density, j_{lim} is related to the mass transfer coefficient k_m by Equation 6.

$$j_{lim} = \frac{i_{lim}}{A} = zFC_{i,b}k_m \quad (6)$$

Current-potential curves for the reduction of ferricyanide, protons and nitrite are shown in Figure 5 with the corresponding mass transfer coefficients as a function of the angular rotation rate. Oscillations of current density values occur at potentials where the current is limited by diffusion. Therefore, the values of limiting currents were determined as mean values on these plateaus. The current density observed in the current-potential curves is smooth at low rotation speeds of less than 100 rpm and the oscillation occurs in the range of 200 to 1600 rpm. It is important to note that competing electrocatalytic reactions at the surface of the electrode will contribute to the current density and might lead to the extraction of incorrect mass transfer coefficient values. This, however, is overcome through the coupling of electrochemical methods with analytical tools for product quantification. The mass transfer coefficients for nitrite reduction in Figure 5C, for example, have been obtained through constant potential electrolysis (Supporting Figure S1) at potentials between -1.1 and -1.15 V vs SHE where the Faradaic efficiency for the reduction of nitrite to ammonia is near 100% within experimental error. That is, the competing hydrogen evolution is slow at these potentials, as determined through gas and liquid product quantification.

The change in mass transfer coefficient values as a function of the electrode rotation speed is not only a function of the flow regime (laminar or turbulent flow) and the molecular properties of the material being transported but these are also a function of the intensive properties of the fluids (i.e., temperature, viscosity, density). Figure 5, for example, shows that mass transfer coefficients for protons are larger than for ferricyanide or nitrite substrates. Likewise, mass transfer coefficients decrease at lower temperatures (Figure 5C) for the same rotation speeds due to changes in diffusion

coefficients, viscosity and density of the electrolyte with temperature. Changes in mass transport also affect local environments at the electrode/electrolyte interface and thus changes in current densities at even low overpotentials are a complex result of changes on surface coverage, local pH, and the local concentration and mean lifetime of reaction intermediates in the proximity of the electrode. All these relations have been thoroughly investigated in the past not only for mass but also for heat transport and have been carefully explained using dimensionless analysis. It is important to recognize at this point that although electrode rotation speeds, gas bubbling flowrates or stirring rates might be intuitive to most electrochemists, these are difficult to translate into the engineering and scale-up of electrocatalytic systems.[9, 10] Dimensionless Analysis should thus be the preferred method of developing functional relationships to describe electrochemical processes, their modeling and scale-up or scale-down.[11]

In dimensionless analysis there is no length, no mass and no time, therefore there are no scale-up problems because there is no scale. Scale-up, then, is simple: express the process using a complete set of dimensionless numbers and try to match them at various scales. The use of electrochemical cells where mass transport is well defined is thus the first step towards generating dimensionless data of relevance to future scale-up efforts.

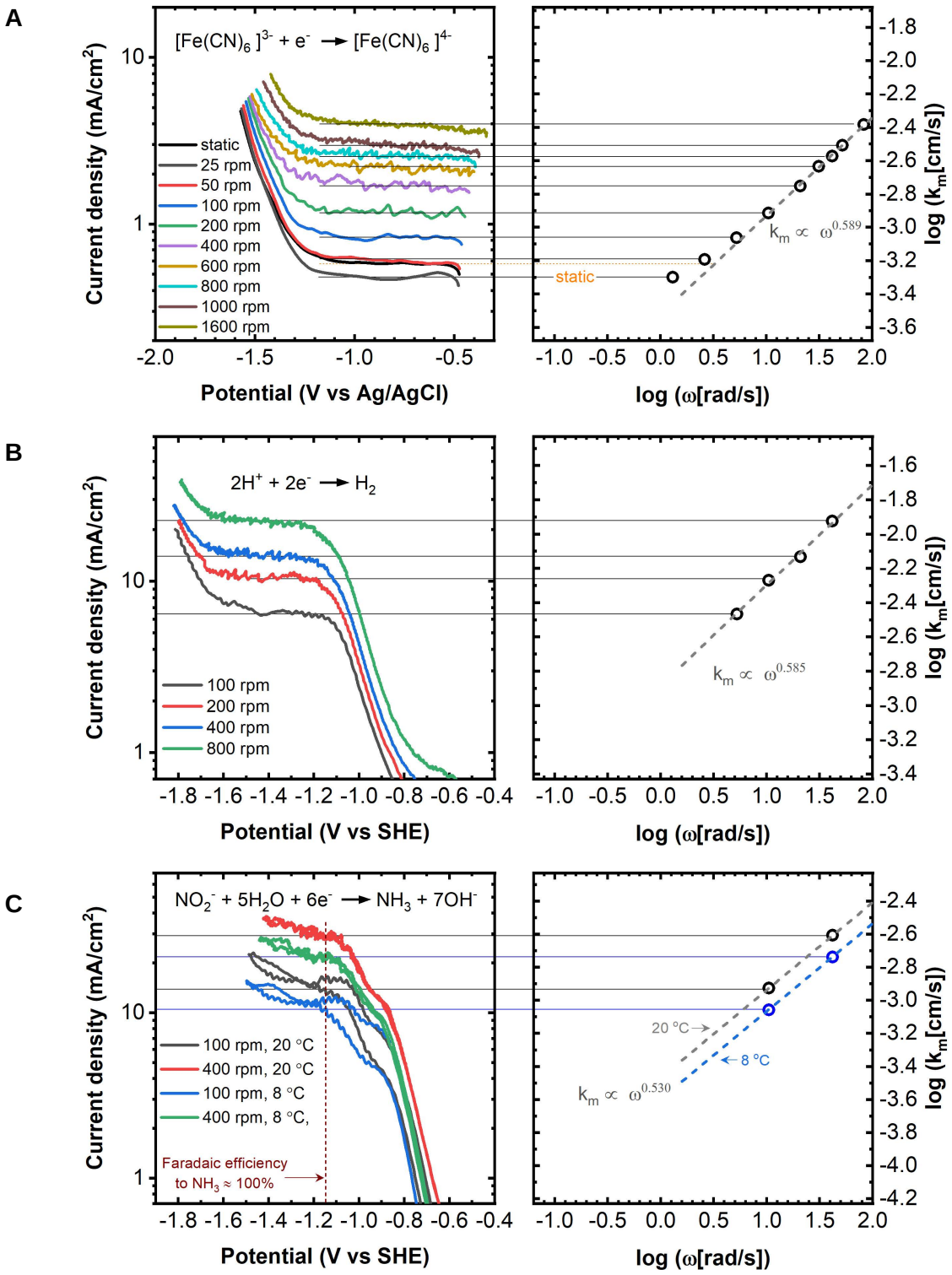

Figure 5. Determination of mass transfer coefficient k_m as function of electrode rotation speed during the reduction of **A)** 10 mM $K_3[Fe(CN)_6]$ in 0.1 M $KHCO_3$ solution on a Cu rotating cylinder electrode at 20 ºC, **B)** 10 mM $HClO_4$ and 50 mM $KClO_4$ solution (pH = 2.0) on a Ti rotating cylinder electrode at 20 ºC, and **C)** 20 mM KNO_2 and 0.1 M $KHCO_3$ on a Cu rotating cylinder electrode at 20 ºC and 8 ºC.

In this work, we will start the dimensionless analysis of the mass transport properties of the RCE cell by calculating the Sherwood number Sh which represents the ratio of the convective mass transfer to the rate of diffusive mass transport. The Sherwood number is the dimensionless version of the mass transfer coefficient and is given by Equation 7 for the ferricyanide, nitrite and proton reduction experiments. The Sherwood number, according to Buckingham's theorem[12], depends only on two important dimensionless groups that describe the system: the Reynolds number Re and the Schmidt number Sc.

$$Sh_{RCE} = \frac{k_m}{D/d_{cyl}} = 0.204 {Re_{RCE}}^{0.59} Sc^{0.33} \quad (7)$$

The empirical relation in Equation 7 holds true even for experiments carried out at different temperatures as the Schmidt number Sc allows the normalization of effects brought about by changes in the ratio of momentum and mass transfer at different temperatures. The Schmidt number is defined as the ratio between the kinematic viscosity of a fluid and the diffusion coefficient of a molecule according to Equation 8:

$$Sc = \frac{\nu}{D} = \frac{\mu}{\rho D} \quad (8)$$

The relation between the Sherwood number and the Schmidt and Reynolds number has been experimentally determined for the RCE cell in this work and is shown in Figure 6A. The Sherwood number for Reynolds numbers between 500 and 12,000 is well described by Equation 7 for large Schmidt numbers of over 100, while at lower Reynold numbers the mixing caused by the constant bubbling of the gas through the electrolyte results in poorly defined mass transport properties even while the electrode is static or being rotated at low speeds ($Re < 500$). Most of the electrocatalytic results reported in the literature, where product detection and quantification are carried out for the

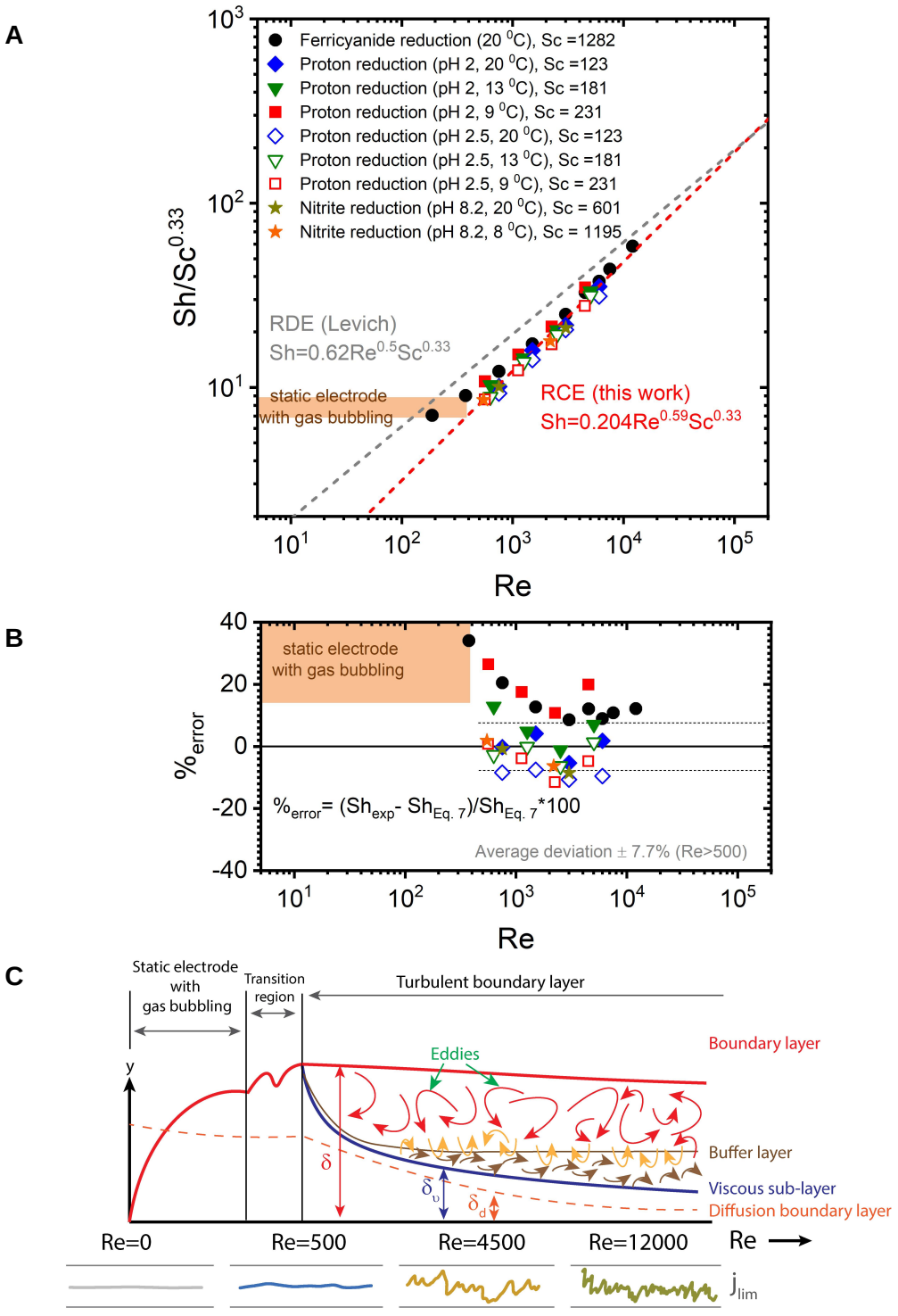

Figure 6. Mass transport characteristics of RCE cell in this work. (A) Plot of log $Sh/Sc^{0.33}$ vs log Re. Dotted lines are the theoretical relations for the RCE in this work and the RDE electrode as determined by Levich. (B) Percentage error between experimentally determined Sh number and $Sh=0.204Re^{0.59}Sc^{0.33}$. (C) Development of Boundary layer over the RCE and its transition to turbulent flow. Diagram not to scale.

transformation of small molecules such as CO_2, N_2 and CH_4 have been obtained in H-type cells where the electrode is static and where gas is bubbled in the bulk of the electrolyte. These conditions are likely to resemble the conditions at the lower Reynolds number in Figure 6A where mass transport is poorly defined and cannot be precisely characterized as either laminar or turbulent. The relation between these three dimensionless groups is in agreement with those observed by others in the past for rotating cylinder electrodes[13, 14] where the Sherwood number is of the form $Sh = KRe^{2/3}Sc^{1/3}$. The average deviation from the experimentally measured Sh number with the general correlation in Equation 7 is ±7.7% for $Re > 500$ (Figure 6B) while the maximum deviation is ~20%.

Considering Levich's discussion of turbulent mass transfer, the dependency of the Sherwood number as a power of ~2/3 with respect to the Reynolds number and 1/3 with respect to the Schmidt number indicate that the penetration of eddies into the laminar sublayers play an important role in the mechanism of the mass transfer[15] in the rotating cylinder electrode for $Re > 500$ in the turbulent regime. That is, the mass transfer coefficient is a function of the diffusivity and viscosity of the system and is also a function of the distance from the solid surface. Accordingly, mass transfer near the surface of the rotating cylinder electrode can be better understood through the description of three different layers each with a uniquely predominant mode of mass transfer. Near the surface of the electrode, the electrolyte in contact with the surface is in a non-slip condition and results in a quasi-static laminar sublayer or viscous sublayer where the predominant mode of mass transfer is diffusion. Aqueous electrolytes under the conditions studied here with the Schmidt number greater than 100 result in viscous

sublayers δ_v in the order of a few tens to a few hundred μm in thickness where the mass diffusion boundary layer δ_d is very thin and will be embedded deep in the hydrodynamic viscous sublayer. The thickness of both the viscous sublayer and the mass diffusion boundary layer is a function of the Reynolds number and decreases in size as the Reynolds number increases. This is schematically shown in Figure 6C. Likewise, the boundary layer thickness δ at $Re > 500$ decreases slowly in size as the rotation speed of the electrode increases and the turbulent flow starts to dominates mass transport. The amplitude of the fluctuations in current shown at the bottom of Figure 6C corresponds to those of the limiting current in the ferricyanide reduction experiments in Figure 5A at different Re values. As the rotation speed and Re values increase the frequency of the current fluctuations increases and the amplitude decreases.

For the sake of comparison, the relation for the Sherwood number in a rotating disk electrode is given in Equation 9.

$$Sh_{RDE} = \frac{k_m}{D/r_{disk}} = 0.62{Re_{RDE}}^{0.5} Sc^{0.33} \quad (9)$$

Here, the Reynold number for the RDE is given by Equation 10.

$$Re_{RDE} = \omega {r_{disk}}^2 \frac{\rho}{\mu} \quad (10)$$

An important frame of reference can be obtained when comparing RCEs and RDEs for the same angular rotation velocity ω. The ratio of the Reynolds numbers for the two is:

$$\frac{Re_{RCE}}{Re_{RDE}} = \frac{{d_{cyl}}^2}{2{r_{disk}}^2} \quad (11)$$

Thus, for a typical cylinder of $d_{cyl} = 12mm$ and a disk of $r_{disk} = 2.5mm$, the Reynolds numbers accessed by the RCE are 11.5 times larger than for the RDE at the same angular rotation while the Sherwood numbers are just approximately 1 to 2 times larger for the RCE than for the RDE. It must be noted, however, that the rotating cylinder electrode geometry is superior to rotating disk electrodes as the electrochemically active surface areas are larger, the primary current distribution is uniform (this is not the case in RDEs), and the hydrodynamics simulate a large range of industrial flow situations.[16-19] Indeed, RCEs have been used at industrial scales[20-24] which has led earlier electrochemical engineers to regret the reversion to the use of RDEs in the study of electrode kinetics as information gathered in these disks is not relevant to industrialization.[16, 19, 25]

3.2 Towards Decoupling Mass Transport and Intrinsic Kinetics

As proof of principle, we have used the gastight RCE system to decouple and rationalize the less-understood mass transport phenomena involved in the electrocatalytic transformation of CO_2, although the same approach can be applied to studying the electrocatalytic transformation of other small molecules such as CO, H_2, N_2, NH_3, O_2 or CH_4. Because the mass transport in the RCE cell is well characterized, we can quantitatively describe the changes in concentration of species near the surface of the electrode through the use of dimensionless quantities and thus simplify the characterization of the electrochemical CO_2 reduction (CO_2R) system with multiple interacting physical and chemical phenomena.

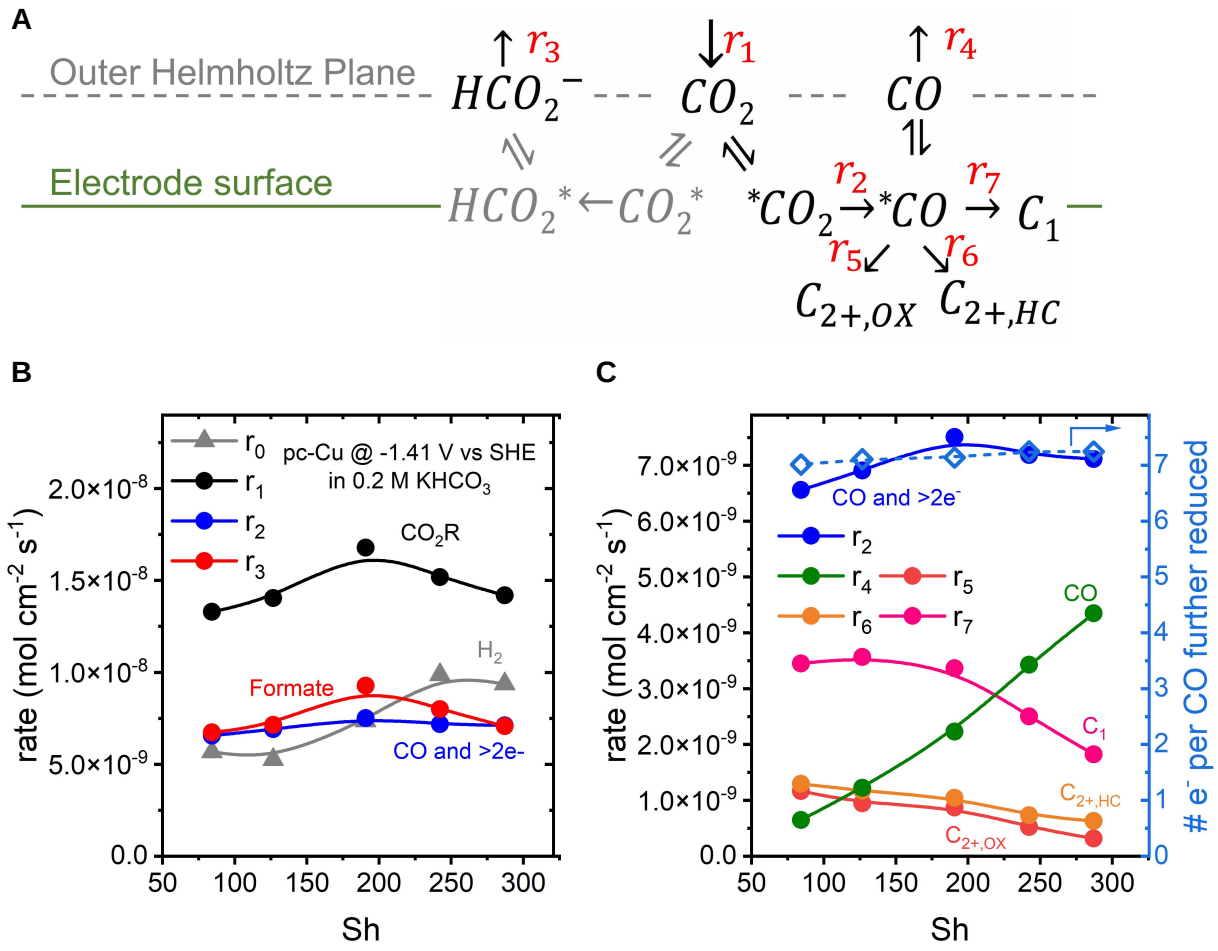

Figure 7. A) Simplified mechanism for CO_2 reduction on a pc-Cu electrode surface showing the CO and formate pathway where CO can be further reduced to C_1 and C_{2+} oxygenates and hydrocarbons. **B)** Experimental rates measured for the production of hydrogen (r_0), formate (r_3) and CO and further reduced products (r_2) at a fixed potential of -1.41V vs SHE as a function of the Sh number. **C)** Breakdown of the rates of CO being further reduced to >2e- products as a function of the Sh number. Right axis shows the average number of electrons per CO molecule in further reduced products. Here, all production rates for CO_2R products are calculated per CO_2 molecules consumed, and the Sh number is calculated using Eq. 7 where Sc=570 for CO.

The study of electrochemical CO_2 reduction systems is not new. The electrochemical reduction of CO_2 on flat polycrystalline copper (pc-Cu) electrodes was first studied by Hori *et al.* in the 1980s.[26-28] Over the last decade, this electrocatalytic transformation has become hugely popular,[1, 29] yet, there is no definitive kinetic reaction mechanism.[30-33] Cu is known to produce carbon monoxide as the key intermediate towards further

reduced hydrocarbons and oxygenated products while formate is known to be a terminal product as illustrated in the simplified reaction network in Figure 7A.[29] New electrode synthesis methods from oxide-derived materials[34] to nanoparticle catalysts[35-37] have been developed and used in the study of Cu electrocatalysts to elucidate the reaction mechanism and the nature of the active sites. Despite these efforts, the proposed mechanisms for CO_2R still remain controversial as mass transport effects have not been taken into account in fundamental electrocatalytic studies.[1, 4, 32, 38-45]

Using the gas-tight RCE cell reported here we can now confidently study CO_2R electrocatalysis to decouple mass transport effects from intrinsic kinetics. Figure 7B shows the changes in rates of CO_2 transformation in mol cm^{-2} s^{-1} to the two main groups of products (r_2 is for CO and further reduced products and r_3 for formate) against the Sh number while holding a flat pc-Cu cylinder electrode at a constant potential of -1.41 V vs SHE in a 0.2 M $KHCO_3$ solution. Here, r_0 is the rate of the competing hydrogen evolution reaction. The first observation is that at -1.41 V vs SHE, the production of hydrogen increases with the increase in the Sh number likely due to the improved mass transport of the bicarbonate buffer, the lowering of the local pH, and the increase in availability of free protons at the outer Helmholtz plane (OHP). The second observation is that the CO and formate pathways do not depend in the same manner on the Sh number. While the CO pathway is independent of the Sh number, the formate pathway is mass transport limited and increases as Sh increases from 80 to 300 reaching a maximum rate at around a Sherwood number of 200. The reasons for the decrease in formate production at the highest Sh number limit is unknown but highlights the need to introduce mass transport effects in theoretical electrocatalysis as the difference in the

CO and formate pathways are currently believed to arise from differences in CO_2 binding modes on the surface of copper[46, 47] while the experiments in the RCE cell suggest that these pathways do not depend on the local CO_2 concentration in the same manner. Therefore, complex relations that arise with changes in the local CO, bicarbonate and hydroxyl concentrations must be considered even for the formate pathway as these could be responsible for the changes in the observed rates of production.

The quantification of gas and liquid products in experiments where mass transport is well-defined allows the further breakdown of complex reaction mechanism involving multiple reaction intermediates. Figure 7C separates the products generated through the CO pathway into CO and its further reduced product families: C_1, and C_{2+} hydrocarbon and oxygenated products. Although some relations appear obvious such as the proportional increase in CO production as it is transported away from the surface at higher Sh values, most relations are complex and nonlinear.[48] Figure 7C shows that pc-Cu is more selective for C-C coupled products (e.g. ethylene and ethanol) at low Sh numbers where mass transfer coefficients are lower and thus the local pH near the surface of the electrode is higher and the concentrations of bicarbonate are low. On the other hand, C_1 products (predominantly methane) production rates remain constant with the improved transport of mass to the electrode up to Sh values of ~200 and then decrease linearly afterwards. Thus, two clear groups of products can be identified. One that groups products with low electron transfer step numbers (2 e^- per molecule) which are favored at higher Sh numbers (H_2, formate and CO), and a second group that contains products with more electron transfer steps per carbon atom (>2e^-) including

ethylene and ethanol which are favorable at low Sh numbers. When counting the number of electrons transferred at -1.41V vs SHE to the CO molecules being further reduced (Figure 7C, right axis) it is evident that the number of electrons transferred per CO molecule remains constant and thus electron-proton coupled steps are not liming at this potential. Lim et al. observed similar changes in gas product selectivity in an RCE setup and proposed that enhanced mass transport of CO away from the electrode surface decrease the coverage of CO and thus hinder the further reduction of CO to hydrocarbons.[48] To understand whether CO coverage is really changing or not, we can estimate the local concentration of CO at the interface in equilibrium with the catalyst surface by assuming that the concentration of CO in the bulk of the electrolyte is zero and that the rate of CO flux out of the electrode (Equation 12) is proportional to the mass transfer coefficient and the Sh number, which are well defined in the RCE cell.

$$r_4 = k_{m,CO} C_{CO,OHP} = \frac{Sh_{RCE} D_{CO}}{d_{cyl}} C_{CO,OHP} \qquad (12)$$

Figure 8A shows the calculated local CO concentration near the surface of the electrode as a function of the Sh number. The calculated CO concentration doubles with the change in the Sh number between 80 and 300. A decrease in CO surface coverage would be expected to result in a lower CO local concentration in equilibrium with the surface which is contrary to the experimental observation where the local concentration of CO increases. It can be hypothesized, however, that improved mass transport shortens the residence time of the produced CO molecules in very close proximity to the electrode surface and thus these CO molecules are less likely to re-adsorb or react directly with other *CO species adsorbed on the surface to form further reduced

products. It cannot be concluded, however, whether the CO coverage is decreasing or not at this very negative fixed potential as lower CO coverages would be expected to result in an increase in availability of active sites and thus the enhancement in the rate of CO_2 reduction to CO and other >2e$^-$ products which is contrary to the experimental observation of r_2 remaining rather constant across all Sh values studied (Figure 7C). Multi-scale modeling of the 3D fluid dynamics and mass transport in the cell along with improved double layer electrochemical models could shine light on the degree of back mixing caused by the penetration of eddies in the viscous sub-layer and the dependance of C-C coupling rates on the CO local concentrations and the mean residence time of intermediates near the surface of the electrode. Modeling, however, is beyond the scope of this work but dimensionless analysis is still valuable enough to provide insight on the role of mass transport in the CO_2 reduction kinetics.

The Damköhler numbers, for example, can be used to rationalize the ratio between mass transfer and reaction time scales. The first Damköhler number (Da_{I,CO_2}, Equation 13) is relevant to understanding CO_2 consumption kinetics at the surface of the electrode as CO_2 is being transported from the bulk of the electrolyte through convection. In Equation 13, r_1 is the rate of CO_2 consumption at the surface of the electrode. It is noted, however, that the Damköhler number calculated in Equation 13 results in a slight underestimation of the CO_2 consumption rate at these potentials as it does not account for chemical reactions in the electrolyte where CO_2 reacts with hydroxyl anions to form bicarbonate.[49, 50]

$$Da_{I,CO_2} = \frac{CO_2\ surface\ consumption\ rate}{CO_2\ convective\ mass\ transfer} = \frac{r_1}{k_{m,CO_2} C_{CO_2,bulk}} \quad (13)$$

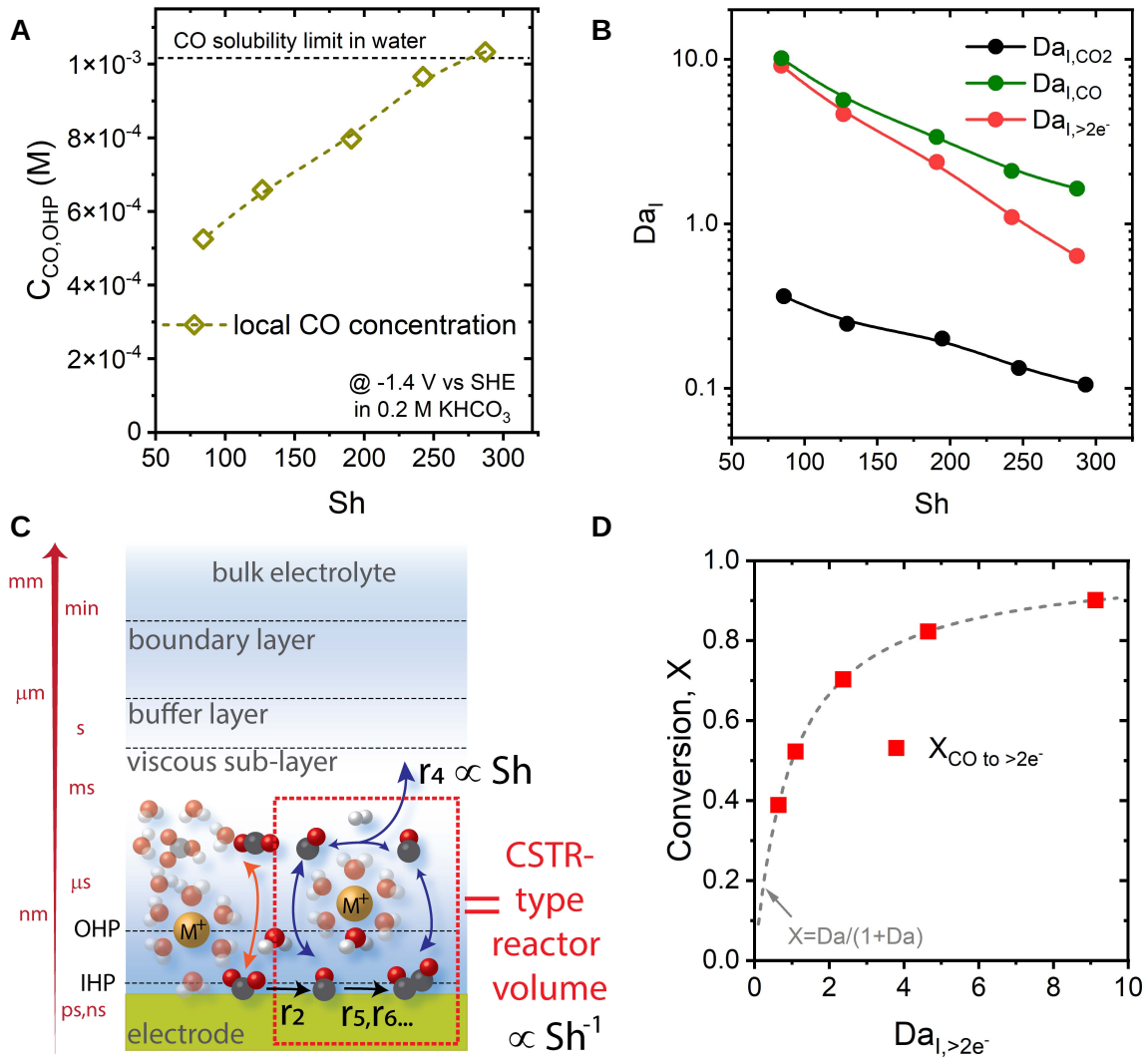

Figure 8. A) Calculated local CO concentration at the Outer Helmoltz Plane as a function of the Sh number at -1.41V vs SHE. **B)** Experimentally determined Damköhler number for CO_2 reduction to CO and further reduced products (Da_{I,CO_2}), CO production and transport away from the electrode ($Da_{I,CO}$), and CO further reduction to >2e$^-$ reduction products ($Da_{I,>2e^-}$). **C)** Schematic representation of a CSTR-type reaction volume at the electrode-electrolyte interface where CO production, desorption, diffusion and further reduction take place within the viscus sub-layer and are affected by the mass transport within the cell as described by the Sh number. **D)** Conversion of CO to further reduced products as function of $Da_{I,>2e^-}$.

The $Da_{I,CO2}$ (Figure 8B) decreases from 0.36 to 0.1 as the Sh number increases. A Damköhler number smaller than 1 indicates that convective mass transport is fast relative to CO_2 consumption at the electrode and thus CO_2 mass transport is not significantly limiting at this potential. This explains why the rate of reduction of CO_2 to

CO and further reduced products on the surface of the electrode is not affected by the Sh number. To understand the change in selectivity down the CO pathway, we can calculate the first Damköhler number for CO as it is being produced on the surface of the electrode (r_2) and as it is being transported away in the RCE cell (r_4) using Equation 14.

$$Da_{I,CO} = \frac{CO\ surface\ production\ rate}{CO\ convective\ mass\ transfer} = \frac{r_2}{r_4} = \frac{r_2}{k_{m,CO} C_{CO,OHP}} \quad (14)$$

The $Da_{I,CO}$ is larger than 1 in the Sh range studied here (Figure 8B) and thus CO is being produced at the surface of the electrode at a rate that is faster than the convective transport of CO out of the boundary layer. The $Da_{I,CO}$ value decreases from 10 to ~1.6 as the Sh number increases, and this explains the linear relation between Sh and r_4 in Figure 7C. That is, because the concentration of CO near the surface of the electrode can be calculated from experimentally measured rates and it is near the saturation limit (Figure 8A), the increase in the mass transfer coefficient with the increase in the Sh number leads to a linear increase in the flux of CO out of the cell which is experimentally measured as r_4. Because CO is slowly being transported away from the electrode, it can diffuse back to the catalyst surface and be further reduced. The probability of CO returning to the surface however decreases as $Da_{I,CO}$ approaches a value of 1 which implies that CO is being transported away at a similar rate at which it is being produced.

The experimental observation that the convective mass transport of CO in the RCE cell is a first-order process at this applied potential is enlightening. We can now use the

experimentally measured r_4 as an internal standard rate to understand the reaction order on CO for further reduction pathways.

$$Da_{I,>2e^-} = \frac{CO\ further\ reduction\ rate}{CO\ convective\ mass\ transfer} = \frac{r_5+r_6+r_7}{r_4} \quad (15)$$

The first Damköhler number for the further reduction of CO (Equation 15) relates the rate of CO further reduction relative to its transport away from the electrode. Figure 8B shows that $Da_{I,>2e^-}$ is inversely proportional to Sh^2. This experimental observation can be rationalized if we approximate the CO further reduction as a first-order reaction in a CSTR-type reactor where the reacting volume corresponds to a well-mixed section of the electrolyte at the electrode/electrolyte interface (Figure 8C). In this region near the surface of the electrode the flow velocity is nearly zero, the length of the reactor volume is smaller than the viscous sub-layer and thus the Bodenstein number within this reactor space is close to zero which justifies the assumption of a full back mixing state as that present in an idealized CSTR reactor. The conversion of CO to further reduced products against $Da_{I,>2e^-}$ is plotted in Figure 8D. The further reduction of CO agrees with Equation 16 which is the expected conversion in a CSTR-type system for a first-order reaction.

$$X_{CO} = \frac{Da_{I,>2e^-}}{1+Da_{I,>2e^-}} = \frac{r_5+r_6+r_7}{r_2} \quad (16)$$

The Damköhler number for a first-order reaction in a CSTR-type reactor is given by Equation 17 and thus although we cannot experimentally separate the values of the CO reduction reaction kinetic constant k and the mean residence time τ from the data presented here, because the applied potential is held constant, we can rationally attribute the change in CO conversion and further reduction entirely to changes in the

residence time of CO near the surface of the electrode which is solely a function of mass transport.

$$Da_{II,>2e^-} = k\tau \quad (17)$$

In summary, we have demonstrated that the further reduction of CO is a first-order reaction process and that the residence time of CO near the surface of the electrode can be controlled by mass transport. Changes in the residence time of CO, the main reaction intermediate, are sufficient to change product selectivity on a pc-Cu electrode without changing the electrode intrinsic kinetics. This observation has significant implications for the design of nanostructured Cu-based electrodes where the kinetics for CO desorption and reabsorption inside of micro and nanopores is poorly understood.

4. CONCLUSION

The gas-tight rotating electrode cell presented here has been designed to study electrocatalytic transformations under conditions of well-defined mass transport. The rotation of the cylinder electrode can be used to move material to and from the surface of the electrocatalyst in a controlled manner across a broad range of mass transport regimes relevant to industrial electrocatalytic applications. We have demonstrated the combination of dimensionless analysis along with experiments under well-defined condition of mass transport as a powerful approach to the study of energy transformations where the substrate is a small molecule that needs to dissolve and diffuse through a liquid layer. This same approach can be used to understand the role of mass transport in electrocatalytic transformations involving protons, buffers and other charged species. Controlling mass transport allows the tuning of micro-environments,

modification of the mean residence time of reaction intermediates near the surface of the electrode and in the future, it should allow the rational study of electrocatalytic transformation and the decoupling of mass transport from intrinsic kinetics.

The rational improvement of the RCE system and its coupling to analytical tools for the detection of gas and liquid products opens for the first time research avenues for the systematic study of electrocatalysts under controlled conditions of applied potential, mass transfer, temperature and electrolyte pH.

Author contributions

All authors contributed equally to the research and writing of this article. C.G.M.-G. conceived the idea and supervised the work.

Conflict of interests

The authors declare no conflict of interest.

Acknowledgements

C.G.M.-G. would like to thank the ALFRED P. SLOAN FOUNDATION for financial support through the award No. G-2021-14160. C.G.M.-G. also acknowledges financial support from the Department of Energy through the award No. DE-EE0007613.

References

1. Kuhl, K.; Cave, E.; Abram, D.; Jaramillo, T., New insights into the electrochemical reduction of carbon dioxide on metallic copper surfaces. *Energy & Environmental Science* **2012,** *5* (5), 7050-7059.
2. Jouny, M.; Lv, J.; Cheng, T.; Ko, B.; Zhu, J.; Goddard, W.; Jiao, F., Formation of carbon-nitrogen bonds in carbon monoxide electrolysis. *Nature Chemistry* **2019,** *11* (9), 846-851.
3. Ross, M.; De Luna, P.; Li, Y.; Dinh, C.; Kim, D.; Yang, P.; Sargent, E., Designing materials for electrochemical carbon dioxide recycling. *Nature Catalysis* **2019,** *2* (8), 648-658.

4. Kas, R.; Yang, K.; Bohra, D.; Kortlever, R.; Burdyny, T.; Smith, W., Electrochemical CO2 reduction on nanostructured metal electrodes: fact or defect? *Chemical Science* **2020,** *11* (7), 1738-1749.
5. Moreno-Garcia, P.; Kovacs, N.; Grozovski, V.; Galvez-Vazquez, M.; Vesztergom, S.; Broekmann, P., Toward CO2 Electroreduction under Controlled Mass Flow Conditions: A Combined Inverted RDE and Gas Chromatography Approach. *Anal. Chem.* **2020,** *92* (6), 4301-4308.
6. Jung, S.; Kortlever, R.; Jones, R.; Lichterman, M.; Agapie, T.; McCrory, C.; Peters, J., Gastight hydrodynamic electrochemistry: Design for a hermetically sealed rotating disk electrode cell. *Anal. Chem.* **2017,** *89* (1), 581-585.
7. Schwammlein, J.; Pham, N.; Mittermeier, T.; Egawa, M.; Bonorand, L.; Gasteiger, H., Through-Plane Conductivity of Anion Exchange Membranes at Sub-Freezing Temperatures-Hydroxide vs (Bi-)Carbonate Ions. *Journal of the Electrochemical Society* **2020,** *167* (8).
8. Clark, E.; Resasco, J.; Landers, A.; Lin, J.; Chung, L.; Walton, A.; Hahn, C.; Jaramillo, T.; Bell, A., Standards and Protocols for Data Acquisition and Reporting for Studies of the Electrochemical Reduction of Carbon Dioxide. *ACS Catal.* **2018,** *8* (7), 6560-6570.
9. Bahari, M.; Roberts, M.; Watt, G.; Harb, J., Mathematical and Experimental Analysis of the Rate Performance of Viologen-Mediated Glucose Fuel Cells. *Journal of the Electrochemical Society* **2020,** *167* (15).
10. Corral, D.; Feaster, J.; Sobhani, S.; DeOtte, J.; Lee, D.; Wong, A.; Hamilton, J.; Beck, V.; Sarkar, A.; Hahn, C.; Jaramillo, T.; Baker, S.; Duoss, E., Advanced manufacturing for electrosynthesis of fuels and chemicals from CO2. *Energy & Environmental Science* **2021,** *14* (5), 3064-3074.
11. Levin, M., How to scale up scientifically. *Pharmaceutical technology* **2005,** *26*, 4-13.
12. Sonin, A. A., A generalization of the Π-theorem and dimensional analysis. *Proceedings of the National Academy of Sciences of the United States of America* **2004,** *101* (23), 8525.
13. Matić, D. J.; Lovreček, B.; Skansi, D., The rotating cylinder electrode. *J. Appl. Electrochem.* **1978,** *8* (5), 391-398.
14. Arvia, A. J.; Carrozza, J. S. W.; Marchiano, S. L., On the mechanism of turbulent flow in mass-transfer controlled electrochemical reactions. *Electrochimica Acta* **1964,** *9* (11), 1483-1495.
15. Levich, V. G., *Physicochemical Hydrodynamics*. Prentice-Hall Inc.: 1962.
16. Gabe, D.; Wilcox, G.; Gonzalez-Garcia, J.; Walsh, F., The rotating cylinder electrode: its continued development and application. *J. Appl. Electrochem.* **1998,** *28* (8), 759-780.
17. Gabe, D. R.; Walsh, F. C., The Rotating Cylinder Electrode - a Review of Development. *J. Appl. Electrochem.* **1983,** *13* (1), 3-22.
18. Eisenberg, M.; Tobias, C. W.; Wilke, C. R., Ionic Mass Transfer and Concentration Polarization at Rotating Electrodes. *Journal of the Electrochemical Society* **1954,** *101* (6), 306-320.
19. Newman, J., Engineering Design of Electrochemical Systems. *Industrial and Engineering Chemistry* **1968,** *60* (4), 12-&.
20. Walsh, F.; Kear, G.; Nahle, A.; Wharton, J.; Arenas, L., The rotating cylinder electrode for studies of corrosion engineering and protection of metals-An illustrated review. *Corrosion Science* **2017,** *123*, 1-20.
21. Walsh, F. C.; Pletcher, D., Electrochemical Engineering and Cell Design. *Developments in Electrochemistry* **2014**, 95-111.
22. Walsh, F. C., The Performance of a 500 Amp Rotating Cylinder Electrode Reactor .3. Methods for the Determination of Mass-Transport Data and the Choice of Reactor Model. *Hydrometallurgy* **1993,** *33* (3), 367-385.
23. Gabe, D. R.; Walsh, F. C., Enhanced Mass-Transfer at the Rotating Cylinder Electrode .3. Pilot and Production Plant-Experience. *J. Appl. Electrochem.* **1985,** *15* (6), 807-824.
24. Walsh, F. C.; Gabe, D. R., Controlled-Potential Electrodeposition of Metals at a Rotating Cylinder Electrode (the Eco-Cell). *Surface Technology* **1981,** *12* (1), 25-37.

25. Newman, J.; Balsara, N. P., Newman and Balsara on Electrochemical Systems Fourth Edition. *Electrochemical Society Interface* **2021,** *30* (1), 11-12.
26. Hori, Y.; Murata, A.; Takahashi, R., Formation of Hydrocarbons in the Electrochemical Reduction of Carbon-Dioxide at a Copper Electrode in Aqueous-Solution. *Journal of the Chemical Society-Faraday Transactions I* **1989,** *85*, 2309-2326.
27. Hori, Y.; Vayenas, C.; White, R.; GamboaAldeco, M., Electrochemical CO2 Reduction on Metal Electrodes. *Modern Aspects of Electrochemistry, No 42* **2008,** (42), 89-189.
28. Hori, Y.; Takahashi, R.; Yoshinami, Y.; Murata, A., Electrochemical reduction of CO at a copper electrode. *Journal of Physical Chemistry B* **1997,** *101* (36), 7075-7081.
29. Nitopi, S.; Bertheussen, E.; Scott, S.; Liu, X.; Engstfeld, A.; Horch, S.; Seger, B.; Stephens, I.; Chan, K.; Hahn, C.; Norskov, J.; Jaramillo, T.; Chorkendorff, I., Progress and Perspectives of Electrochemical CO2 Reduction on Copper in Aqueous Electrolyte. *Chem. Rev.* **2019,** *119* (12), 7610-7672.
30. Perez-Gallent, E.; Figueiredo, M. C.; Calle-Vallejo, F.; Koper, M. T., Spectroscopic Observation of a Hydrogenated CO Dimer Intermediate During CO Reduction on Cu(100) Electrodes. *Angew Chem Int Ed Engl* **2017,** *56* (13), 3621-3624.
31. Perez-Gallent, E.; Marcandalli, G.; Figueiredo, M.; Calle-Vallejo, F.; Koper, M., Structure- and Potential-Dependent Cation Effects on CO Reduction at Copper Single-Crystal Electrodes. *Journal of the American Chemical Society* **2017,** *139* (45), 16412-16419.
32. Kortlever, R.; Shen, J.; Schouten, K.; Calle-Vallejo, F.; Koper, M., Catalysts and Reaction Pathways for the Electrochemical Reduction of Carbon Dioxide. *Journal of Physical Chemistry Letters* **2015,** *6* (20), 4073-4082.
33. Garza, A. J.; Bell, A. T.; Head-Gordon, M., Mechanism of CO2 Reduction at Copper Surfaces: Pathways to C2 Products. *ACS Catal.* **2018,** *8* (2), 1490-1499.
34. Roberts, F.; Kuhl, K.; Nilsson, A., High Selectivity for Ethylene from Carbon Dioxide Reduction over Copper Nanocube Electrocatalysts. *Angew. Chem. Int. Ed.* **2015,** *54* (17), 5179-5182.
35. Kim, D.; Kley, C.; Li, Y.; Yang, P., Copper nanoparticle ensembles for selective electroreduction of CO2 to C-2-C-3 products. *Proceedings of the National Academy of Sciences of the United States of America* **2017,** *114* (40), 10560-10565.
36. Yu, F.; Wei, P.; Yang, Y.; Chen, Y.; Guo, L.; Peng, Z., Material design at nano and atomic scale for electrocatalytic CO2 reduction. *Nano Materials Science* **2019,** *1* (1), 60-69.
37. Loiudice, A.; Lobaccaro, P.; Kamali, E. A.; Thao, T.; Huang, B. H.; Ager, J. W.; Buonsanti, R., Tailoring Copper Nanocrystals towards C2 Products in Electrochemical CO2 Reduction. *Angewandte Chemie International Edition* **2016,** *55* (19), 5789-5792.
38. Schouten, K. J. P.; Kwon, Y.; van der Ham, C. J. M.; Qin, Z.; Koper, M. T. M., A new mechanism for the selectivity to C1 and C2 species in the electrochemical reduction of carbon dioxide on copper electrodes. *Chemical Science* **2011,** *2* (10), 1902-1909.
39. Nie, X.; Luo, W.; Janik, M. J.; Asthagiri, A., Reaction mechanisms of CO2 electrochemical reduction on Cu(111) determined with density functional theory. *J. Catal.* **2014,** *312*, 108-122.
40. Wang, L.; Nitopi, S.; Bertheussen, E.; Orazov, M.; Morales-Guio, C.; Liu, X.; Higgins, D.; Chan, K.; Norskov, J.; Hahn, C.; Jaramillo, T., Electrochemical carbon monoxide reduction on polycrystalline copper: Effects of potential, pressure, and pH on selectivity toward multicarbon and oxygenated products. *ACS Catal.* **2018,** *8* (8), 7445-7454.
41. Liu, X.; Xiao, J.; Peng, H.; Hong, X.; Chan, K.; Nørskov, J. K., Understanding trends in electrochemical carbon dioxide reduction rates. *Nature communications* **2017,** *8* (1), 1-7.
42. Todorova, T.; Schreiber, M.; Fontecave, M., Mechanistic Understanding of CO2 Reduction Reaction (CO2RR) Toward Multicarbon Products by Heterogeneous Copper-Based Catalysts. *ACS Catal.* **2020,** *10* (3), 1754-1768.

43. Zhu, S.; Li, T.; Cai, W.; Shao, M., CO2 electrochemical reduction as probed through infrared spectroscopy. *ACS Energy Lett.* **2019,** *4* (3), 682-689.
44. Liu, X.; Schlexer, P.; Xiao, J.; Ji, Y.; Wang, L.; Sandberg, R.; Tang, M.; Brown, K.; Peng, H.; Ringe, S.; Hahn, C.; Jaramillo, T.; Norskov, J.; Chan, K., pH effects on the electrochemical reduction of CO(2) towards C-2 products on stepped copper. *Nature Communications* **2019,** *10*.
45. Hussain, J.; Jónsson, H.; Skúlason, E., Calculations of Product Selectivity in Electrochemical CO2 Reduction. *ACS Catal.* **2018,** *8* (6), 5240-5249.
46. Feaster, J.; Shi, C.; Cave, E.; Hatsukade, T.; Abram, D.; Kuhl, K.; Hahn, C.; Norskov, J.; Jaramillo, T., Understanding Selectivity for the Electrochemical Reduction of Carbon Dioxide to Formic Acid and Carbon Monoxide on Metal Electrodes. *ACS Catal.* **2017,** *7* (7), 4822-4827.
47. Resasco, J.; Lum, Y.; Clark, E.; Zeledon, J.; Bell, A., Effects of Anion Identity and Concentration on Electrochemical Reduction of CO2. *Chemelectrochem* **2018,** *5* (7), 1064-1072.
48. Lim, C.; Harrington, D.; Marshall, A., Effects of mass transfer on the electrocatalytic CO2 reduction on Cu. *Electrochimica Acta* **2017,** *238*, 56-63.
49. Gupta, N.; Gattrell, M.; MacDougall, B., Calculation for the cathode surface concentrations in the electrochemical reduction of CO2 in KHCO3 solutions. *J. Appl. Electrochem.* **2006,** *36* (2), 161-172.
50. Morales-Guio, C.; Cave, E.; Nitopi, S.; Feaster, J.; Wang, L.; Kuhl, K.; Jackson, A.; Johnson, N.; Abram, D.; Hatsukade, T.; Hahn, C.; Jaramillo, T., Improved CO2 reduction activity towards C2+ alcohols on a tandem gold on copper electrocatalyst. *Nature Catalysis* **2018,** *1* (10), 764-771.